

Surface-directed capillary system; theory, experiments and applications

Salim Bouaidat,^{*ab} Ole Hansen,^b Henrik Bruus,^b Christian Berendsen,^a Niels Kristian Bau-Madsen,^a Peter Thomsen,^a Anders Wolff^b and Jacques Jonsmann^a

Received 15th February 2005, Accepted 6th June 2005

First published as an Advance Article on the web 1st July 2005

DOI: 10.1039/b502207j

We present a capillary flow system for liquid transport in microsystems. Our simple microfluidic system consists of two planar parallel surfaces, separated by spacers. One of the surfaces is entirely hydrophobic, the other mainly hydrophobic, but with hydrophilic pathways defined on it by photolithographic means. By controlling the wetting properties of the surfaces in this manner, the liquid can be confined to certain areas defined by the hydrophilic pathways. This technique eliminates the need for alignment of the two surfaces. Patterned plasma-polymerized hexafluoropropene constitutes the hydrophobic areas, whereas the untreated glass surface constitutes the hydrophilic pathways. We developed a theoretical model of the capillary flow and obtained analytical solutions which are in good agreement with the experimental results. The capillarity-driven microflow system was also used to pattern and immobilize biological material on planar substrates: well-defined 200 μm wide strips of human cells (HeLa) and fluorescence labelled proteins (fluorescein isothiocyanate-labelled bovine serum albumin, *i.e.*, FITC-BSA) were fabricated using the capillary flow system presented here.

1 Introduction

Control of liquid is of principal importance in almost all microfluidic systems.¹ Often mechanical and electric control is used, such as valves,² electrohydrodynamic pumps,^{3,4} electro wetting systems,⁵ pressure-driven membrane pumps,⁶ bubble pumps,⁷ or rotary pumps.⁸ However, a simple way of transporting liquid is by capillary action. Capillarity or capillary action is a common physical phenomenon, where liquids wet the interior of capillaries. The liquid penetrates into for instance narrow tubes, fine pores, cracks or channels due to an energy gain obtained by extending the solid–liquid interface while at the same time reducing the solid–gas interface.⁹ Capillary effects dominate in microfluidics due to the large surface-to-volume ratio.

Conventional capillarity-driven systems consist of closed micro channels, where the liquid is completely confined by walls in all directions perpendicular to the flow. The liquid sample is transported from a reservoir to a waste, and on its way, the liquid can, *e.g.*, be subjected to different reagents or reactions, which can be monitored by a sensor unit.^{10–13} In this paper, a single sided capillarity-driven system is presented. The system, referred to as a surface-directed flow system, is an open-channel system without sidewalls, consisting of parallel top and bottom surfaces separated by a spacer layer, see Fig. 1. The liquid is confined to a hydrophilic pathway on only the bottom surface, without propagating sideways into surrounding hydrophobic areas. Other groups have developed similar surface-directed flow systems,^{14–16} but in these the top and

bottom surfaces had identical hydrophilic pathways which necessitated an accurate alignment procedure. In the system presented here however, only the bottom surface is provided with hydrophilic pathways, whereas the top surface is completely hydrophobic. The need for a tricky alignment of the surfaces is thereby eliminated.

The structure of the paper is as follows: In section 2 we present a theoretical model of the system and an analytical solution for the position of the liquid meniscus as a function of time. The solution is derived from conservation of momentum and from surface energy considerations in a simplified geometry and under the assumption of ideal Poiseuille flow. In section 3.1 we describe the fabrication of the system, where a plasma-polymerized fluorinated polymer was used as the hydrophobic surface material.^{17–21} The fluorinated coating was deposited on an untreated glass substrate by low-energy plasma polymerization of hexafluoropropene (referred to as

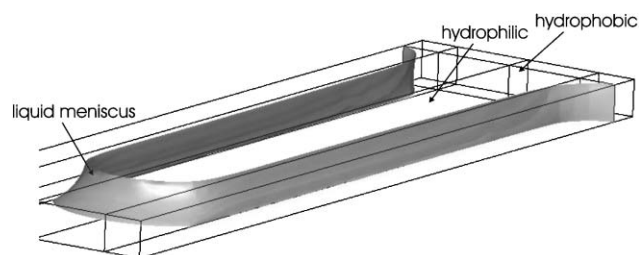


Fig. 1 An open-channel surface-directed flow system. The image, which shows the liquid meniscus after travelling a distance corresponding to five channel widths, originates from a FVM (Finite Volume Method) simulation. The modelling tool CFD-ACE+ was used. The flow system consists of a coated glass substrate (bottom) and lid (top). A hydrophilic pathway, is surrounded by hydrophobic areas on the substrate, whereas the lid is completely hydrophobic. Spacers at the edges (not shown) separate the surfaces.

^aScandinavian Micro Biodevices ApS (SMB), Gammelgårdsvej 87C, DK-3520 Farum, Denmark

^bMIC—Department of Micro and Nanotechnology, Technical University of Denmark, DTU Bldg. 345east, DK-2800 Kgs. Lyngby, Denmark. E-mail: sab@smb.dk

ppHFP). The low plasma energy density is advantageous, since functional groups, such as the fluoro-groups here, are maintained to a higher degree compared to conventional (higher energy) plasmas. The low-energy plasma used in this study was created using low frequency AC, but other methods are possible: pulsed RF,²² CW-RF^{23–25} or DC.²⁶ Hydrophilic pathways were created in the ppHFP by a photolithographic lift-off process that exposed the untreated glass of the substrate.^{27,28} In section 3.2 we describe the measuring setup.

In section 3.3 and 3.4 we extend our system to a biochip. To demonstrate applications of surface-directed flow, other than just liquid transport, the technology was also used to pattern both proteins, in this case fluorescein isothiocyanate-labeled bovine serum albumin (FITC-BSA) and human cells (HeLa) on planar surfaces. Thin protein and cell strips, 200 μm in width, were fabricated on standard format borosilicate glass slides.

In section 4 we present the experimental results, and compare them to our simple model calculations. Finally in section 5 we conclude.

2 Theory

Consider the capillary flow system, shown in Fig. 1, formed by two horizontal, parallel, hydrophobic coated glass plates separated by a distance a . On the lower plate a linear hydrophilic track of length L and width b is formed as shown in Fig. 2. The liquid flowing in this capillary is assumed to have the static contact angles θ_1 and θ_2 on the hydrophilic and hydrophobic surfaces, respectively.

Far from the entry and the end meniscus, the shape of the lateral cross-section of the liquid column in the capillary is expected to be a single circle intersected by the two planar surfaces due to vertical stability, see Fig. 2(b). The contact angle θ_t at the top surface equals the static contact angle, $\theta_t = \theta_2$, due to lateral stability. At the bottom surface, the hydrophilic surface is fully wetted and the meniscus is pinned at the boundaries to the hydrophobic regions. At this boundary, the actual contact angle θ_b is between the two static contact angles for the hydrophobic and hydrophilic surfaces, *i.e.*, $\theta_1 < \theta_b < \theta_2$, as required by geometry. In the limit of the infinitely small separation a of the two glass plates, $\theta_b \approx \pi - \theta_2$. In the following, we will ignore the small effects related to curvature of the liquid–air interface and thus assume

a rectangular lateral cross-section (of width b and height a) of the liquid column.

The horizontal capillary system is connected to the liquid feed volume at position $x = 0$ at the time $t = 0$. At time t the meniscus is at the position x and moves with the speed \dot{x} . The contribution to the total momentum from the liquid in the capillary is $P_{\text{capillary}} = \rho abx\dot{x}$, where the mass density, ρ , of the liquid is assumed to be constant. The contribution to the total momentum from the feed volume can be written as $P_{\text{feed}} \approx \rho \Lambda ab\dot{x}$, where Λ is a characteristic length for the feed volume capillary system. The characteristic length, Λ , is dependent on the feed volume geometry and the flow pattern, but for a hemispherical feed volume a reasonable estimate is $\Lambda \approx R/2$, where R is the radius of the hemisphere. However, on the time scale relevant for the present study this contribution is only of marginal importance. First, because a small feed volume (50 μL) with an estimated characteristic length $\Lambda \approx 1.5$ mm is used (far less than the experimental capillary fill length), second, because inertial effects in general are of minor importance on the experimental time scale ($\Delta t = 0.04$ s). Finally, numerical solution of the full equation of motion has verified the very small influence from the feed volume momentum hence we shall ignore it.

Conservation of momentum is the starting point for the analysis of the dynamics of the capillary flow in the surface-directed flowsystem. The temporal evolution of the total momentum P_{tot} of the fluid is governed by Newton's equation

$$\frac{dP_{\text{tot}}}{dt} = F_c + F_f + F_h \quad (1)$$

where F_c is the capillary force, F_f is the viscous friction force and F_h is the hydrostatic force. If the liquid is considered incompressible, it follows that the equation of motion along the horizontal x -axis becomes

$$\rho ab \frac{d(x\dot{x})}{dt} \approx F_c + F_f \quad (2)$$

The contribution to the total energy of the system due to surface tension is

$$E_\gamma = [2a - b(\cos \theta_1 + \cos \theta_2)] x\gamma_{lv} + bL(\gamma_{s1v} + \gamma_{s2v}) + A_{\text{men}}\gamma_{lv} \quad (3)$$

where Young's equation $\gamma_{lv}\cos \theta_i = \gamma_{siv} - \gamma_{sil}$ ²⁹ has been used to express the energy, primarily in terms of the static contact angles θ_1 and θ_2 between the liquid and surface 1 (the

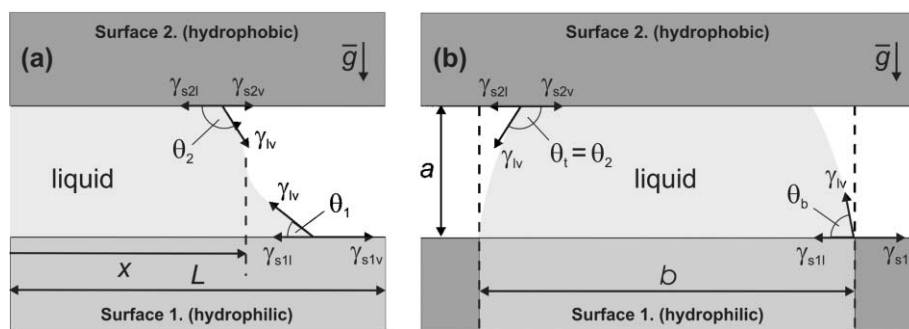


Fig. 2 (a) Cross-sectional side view of a surface-directed flow system with width b , height a and length L (at equilibrium). The solid–liquid, liquid–vapor and solid–vapor surface tensions, defining the contact angles, are also shown at the contact lines. (b) Cross-sectional front view. The liquid is pinned at the vapor–liquid interface with an outward circular curvature (at equilibrium). The gravitational acceleration \vec{g} is marked.

hydrophilic surface) and surface 2 (the hydrophobic surface) respectively, and the surface tension γ_{lv} of the liquid. γ_{s1v} and γ_{s2v} are the surface tensions of the two dry solid surfaces 1 and 2, see Fig. 2(a). A_{men} is the area of the front meniscus at x . If A_{men} is assumed to be independent of the position of the meniscus, the capillary force is independent of the filling of the capillary

$$F_c \equiv -\frac{\partial E_\gamma}{\partial x} = -[2a - b(\cos \theta_1 + \cos \theta_2)]\gamma_{lv} \quad (4)$$

It follows that spontaneous liquid motion (capillary driven flow) will occur if F_c is positive, which requires $2alb < (\cos \theta_1 + \cos \theta_2)$.

The force due to viscous friction F_f can be approximated by assuming Poiseuille flow. The parabolic velocity profile implied results in a uniform shear stress $\tau = 6\eta\langle v \rangle/a$ on the top and bottom plates, where η is the viscosity of the liquid.^{30,31} Since to a good approximation the average flow velocity equals the speed of the meniscus, $\langle v \rangle \simeq \dot{x}$, the viscous force on the liquid is

$$F_f \simeq -12\eta\frac{b}{a}x\dot{x} \quad (5)$$

The parabolic velocity profile implied in the Poiseuille flow is valid in most of the channel. However, in a short transition region near the entrance, where the Poiseuille flow is not yet fully developed, the flow pattern is different, and the viscous drag marginally larger than in the fully developed flow. Likewise, near the front meniscus, the flow pattern is much more complicated and a larger viscous drag is expected. These effects are small enough that the Poiseuille flow assumption can be justified for a first order description of the capillary dynamics. This was confirmed by FVM (Finite Volume Method) simulations, using CFD-ACE+.

Inserting eqns. (4) and (5) into eqn. (2) results in an approximate equation of motion for the meniscus

$$\frac{d^2(x^2)}{dt^2} + \frac{12\eta}{\rho a^2} \frac{d(x^2)}{dt} + \frac{2[2a - b(\cos \theta_1 + \cos \theta_2)]\gamma_{lv}}{\rho ab} = 0 \quad (6)$$

where $d(x^2)/dt = 2x\dot{x}$ has been used. This second order differential equation for fully developed viscous incompressible flow (Poiseuille flow) in a surface-directed flow system is analogous to that of cylindrical capillaries, except that the constants differ.³² Ideally we would impose the initial conditions $x(0) = 0$ and $\dot{x}(0) = 0$ on the equation. However, if the time differentiations in eqn. (6) are carried out and the condition $x(0) = 0$ is imposed, then the remaining terms on the left hand side of the equation are the capillary force term and the term $2(\dot{x})^2$. Thus only the first initial condition can be fulfilled[†], and the initial meniscus speed must be $\dot{x}(0) = \sqrt{[b(\cos \theta_1 + \cos \theta_2) - 2a]\gamma_{lv}/(\rho ab)}$ in order to satisfy eqn. (6). This nonphysical condition, which requires infinite acceleration at $t = 0$, arises because we have ignored the feed volume contribution to the total momentum. If the feed volume momentum is included, a finite initial acceleration results, and the required initial speed for the simplified solution is reached in a time below the time resolution of the experiment. Thus, on the time scale of the experiments this is without significance. The solution to

[†] In eqn. (6) we of course initially fulfil both $x^2 = 0$ and then trivially $d(x^2)/dt = 0$.

the simplified equation is

$$x(t) = \sqrt{\frac{\gamma_{lv}\rho a^3}{72\eta^2 b} [b(\cos \theta_1 + \cos \theta_2) - 2a]} \sqrt{\frac{12\eta}{\rho a^2} t + \exp\left(-\frac{12\eta}{\rho a^2} t\right) - 1} \quad (7)$$

For times longer than the momentum relaxation time of the capillary system, $\tau = \rho a^2/(12\eta)$, the position is approximately given by

$$x(t) \simeq \sqrt{\frac{\gamma_{lv}a}{6\eta b} [b(\cos \theta_1 + \cos \theta_2) - 2a]} (t - \tau), t \gg \tau \quad (8)$$

In order to test the model against experimental data, it is useful to study the behaviour in the long time regime, since the relation

$$\beta \equiv \frac{1}{a} \frac{d(x^2)}{dt} \simeq \frac{\gamma_{lv}}{6\eta} \left[(\cos \theta_1 + \cos \theta_2) - \frac{2a}{b} \right] \quad (9)$$

allows distinction between contact angle errors and other liquid parameter errors if experimental data for different aspect ratios alb are plotted according to eqn. (9). The symbol β defined in eqn. (9) is convenient for the discussions in the experimental section.

The expression for the slope β in eqn. (9) is only valid for a limited range of capillary aspect ratios, $0 < alb \leq -\cot \theta_2$. At an aspect ratio $alb > -\cot \theta_2$ the fluid will start to partly wet the hydrophobic region surrounding the hydrophilic track, and both actual contact angles become equal to the static contact angle of the hydrophobic surface, $\theta_b = \theta_t = \theta_2$. As a result, the capillary force and the slope β decrease at a faster rate with increasing aspect ratio above this value. Moreover, as seen from the simple geometrical considerations, the condition for spontaneous liquid motion becomes somewhat stronger, $alb < c_1/c_2$, where $c_1 = \frac{1}{2}(\cos \theta_1 - \cos \theta_2)$ and $c_2 = [\sin \theta_2 - (2\theta_2 - \pi)/(2\cos \theta_2)]$.

3 Experimental and methods

3.1 Fabrication of the flow cell

500 μm standard boro-silicate glass wafers were used as substrates (bottom) and standard format microscope slides (ProSciTech G 300) were used as lids (top). The boro-silicate wafers and slides were cleaned using piranha [H_2SO_4 (98%) : H_2O_2 (30%), ratio 3 : 1] before processing. The substrates were spin-coated with 4.2 μm thick photoresist (AZ5214E from Clariant), which was patterned using conventional photolithography, see Fig. 3(B), (C) and (D). The lithography involved hotplate baking at 90 $^\circ\text{C}$, UV-exposure, and exposure to a photoresist developer (AZ351B from Hoechst). The coating on the lid was not patterned.

After the photoresist steps, the ppHFP was deposited by plasma polymerization using a simple (50 Hz AC voltage) plasma generation technique. This technique has been described in detail in previous work.^{27,28} The wafers and slides were placed in the plasma chamber and the pressure was decreased to 1.3 Pa. The wafers and slides were then pre-treated in an argon plasma followed by a hydrogen plasma, 10 s each and with a power density of 5 W L^{-1} . The purpose of the argon and hydrogen plasma is to clean and activate the glass

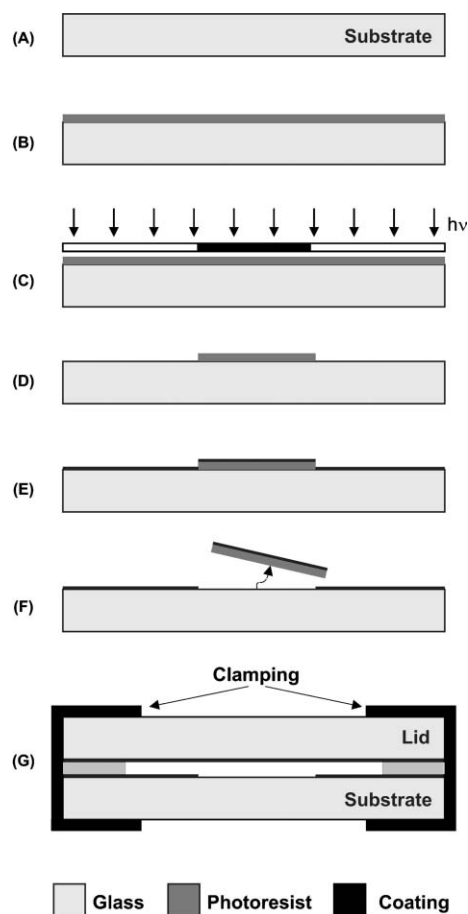


Fig. 3 The process sequence. (A) and (B): 4.2 μm thick photoresist was spun onto a borosilicate substrate. After a short bake, the photoresist was exposed to UV light through a photomask, (C), and parts of the photoresist were dissolved (in this case the exposed parts, *i.e.*, positive-tone) in a photoresist developer, (D). The substrate was then placed in the plasma chamber and ppHexene and ppHFP were deposited by plasma polymerization, (E). The coatings were patterned by lift-off using acetone, (F). Finally, the lid and substrate were tightly clamped together with one or more 15 μm thick tinfoil straps as spacers, (G).

surface, thereby improving adhesion. The power density was subsequently lowered to 2.5 W L^{-1} and a flow of 1-hexene vapor (100 sccm) and argon (20 sccm) was fed into the chamber for 30 s. The hexene (ppHexene) acts as an adhesion layer for the ppHFP. After the deposition of ppHexene, the plasma was stopped, and a flow of hexafluoropropene (>98.5%, supplied by sABCR, Karlsruhe, Germany) was introduced to the chamber (flow rate: 30 sccm). The pressure was then increased to 5 Pa and the power was turned on for 60 s at 4 W L^{-1} . This gave an approximate total thickness of 270 \AA , determined using a QCM (Quartz Crystal Microbalance) during deposition.

Finally, the plasma-polymerized coating on the substrate was lifted using acetone, see Fig. 3(F). Ultrasound for 20 min was used to promote the lift-off.

Lift-off did, however, leave residues of photoresist on the glass surface, which increases the water contact angle on the glass to approximately 55°. To reduce the contact angle

without harming the ppHFP, a fluorine plasma (CF_4) treatment was used. The oxygen plasma (O_2), which is conventionally used to remove photoresist residues, would also etch the thin ppHFP coating within a few seconds. By using a fluorine plasma instead, a longer treatment is possible, thereby removing the photoresist residues and still maintaining a functional ppHFP coating. A TePla 300 Plasma Processor system (from Technics Plasma GmbH) was used with the following process parameters: flow 125 sccm CF_4 , power 100 W, time 1 min and pressure 41 Pa. This process resulted in a contact angle on glass of approximately $21^\circ \pm 5^\circ$, without influencing the contact angle on the ppHFP, which remained at approximately $103^\circ \pm 2^\circ$ (see Table 1).

The lid and substrate were then tightly clamped together using tinfoil straps as spacers, see Fig. 3(G).

3.2 Experimental setup for flow measurements

After tightly clamping the lid and substrate of the surface-directed flow cell together, the flow cell was placed under a Leica MZ125 zoom microscope fitted with a Leica ICA camera. Continuous video recordings were used to determine the position of the liquid meniscus. 50 μL DI water was dispensed at the inlet of the flow cell at every measurement. The flow cell was disassembled and the water removed using compressed nitrogen, after each recording. Each individual recording was repeated four times. After each set of individual recordings, the substrate and lid were cleaned using acetone and ultrasound for 2 min and washed using DI water for 5 min. The CF_4 plasma treatment, mentioned above, was necessary in some cases to reduce the contact angle of the glass further. The contact angle was measured shortly before each set of flow recordings. The spacer distance a was varied by using one or more pieces of tinfoil each 15 μm thick.

The video recordings were then analyzed using the software “Jasc Animation Shop v3.04” (Jasc Software). The position of the liquid meniscus was determined by splitting each recording into frames. The sample rate of video recording equipment was 25 frames s^{-1} , corresponding to a resolution of 0.04 s.

3.3 Human cell culture preparation

Human cells (HeLa, Cat. no. CCL-2) were prepared using the following procedure. The flow cell was exposed to a cell

Table 1 Capillary dimensions and measured water contact angles for four different experiments. The contact angles were measured on glass (corresponding to the hydrophilic pathways) and ppHFP (hydrophobic area) using a FTÅ200 dynamic contact angle analyzer from First Ten Ångströms. The measurements were performed at room temperature and at air humidities between 30–39%RH, using a spherical fit model in the case of ppHFP and a non-spherical fit model in the case of glass. Five measurements were performed in each case at different locations on the surfaces. An average dispense volume of 6 μL was used

Experiment	Capillary dimensions/ μm		Contact angle	
	Height a	Width b	Glass surface	ppHFP
1	15 \pm 1	200	22 \pm 4.2°	104 \pm 1.8°
2	30 \pm 2	200	23 \pm 3.7°	103 \pm 2.2°
3	45 \pm 3	200	22 \pm 4.0°	104 \pm 1.2°
4	15 \pm 1	100	18 \pm 4.9°	104 \pm 0.7°

culture, which had previously been grown in Eagle's Minimal Essential Medium (from LGC Promochem, Sweden) in T75 flasks, with an admixture of Foetal Bovine Serum 10% (v/v) (from ATTC) and Penicillin–Streptomycin–Glutamine (10 U mL⁻¹–10 µg mL⁻¹–2 mM, from Invitrogen, CA). After the cell suspension had reached confluence by incubation at 37 °C and 5% CO₂, the cells were separated from the growth medium using phosphate-buffered saline (PBS) and trypsin–EDTA in HBSS (both from ATTC). To concentrate the cells, the cell suspension was centrifuged at 200 rpm for 30 s, using an Eppendorf 5804R centrifuge, after which the pellet was resuspended with conditioned growth medium. This procedure was repeated. The new suspension (100 µL) was then dispensed at the inlet of the flow cell and allowed to fill the hydrophilic pathways. The flow cell was inspected using a Zeiss 200 m inverted (fluorescence) microscope fitted with a Hamamatsu Orca L7465 digital CCD camera.

LysoTracker Red (DND-99, supplied by Molecular Probes) was diluted in PBS (100 nL mL⁻¹). LysoTracker, which is a red-fluorescent dye that stains acidic compartments in live cells, was used to distinguish living and dead cells.³³

3.4 Protein adsorption preparation

Fluorescent labeled proteins (fluorescein isothiocyanate-labeled bovine serum albumin (FITC-BSA)) were dissolved in PBS (1 mg mL⁻¹), both supplied by Sigma. 50 µL of FITC-BSA–PBS solution was dispensed at the inlet of the flow cell, and the solution was allowed to rest for 30 min in the flow cell. The flow cell was then disassembled and the surfaces washed for 5 min in PBS and 1 min in DI water. The samples were scanned (530 nm) using an array WoRx scanner from AppliedPrecision (fitted with FITC-filters).

4 Results and discussion

4.1 Contact angle

Static, advancing and receding water contact angle measurements of the ppHFP and the borosilicate glass surfaces were performed. The water contact angles were measured using a FTÅ200 dynamic contact angle analyzer from First Ten Ångströms. Measurements were carried out at room temperature, and the DI water used for the measurements was dispensed and retracted at a rate of 60 µL min⁻¹. A typical dynamic contact angle measurement on ppHFP is shown in Fig. 4. The advancing contact angle on ppHFP drops from approximately 115° to 105°, whereas the receding contact angle decreases from 105° down to approximately 82° and increases again to approximately 93°. The increase in the receding contact angle is a geometrical side effect of the measurement method, which occurs when the radius of the droplet becomes comparable to the radius of the feed tube, thus this effect appears at feed volumes that increase with increasing static contact angle of the surfaces. Fig. 4 also shows the advancing and receding contact angle on glass. The graph for glass is much more coarse, compared to the graph for ppHFP. This is due to limitations of the contact angle analyzer. It is inherently difficult to measure low dynamic contact angles. As a consequence, the uncertainties are higher

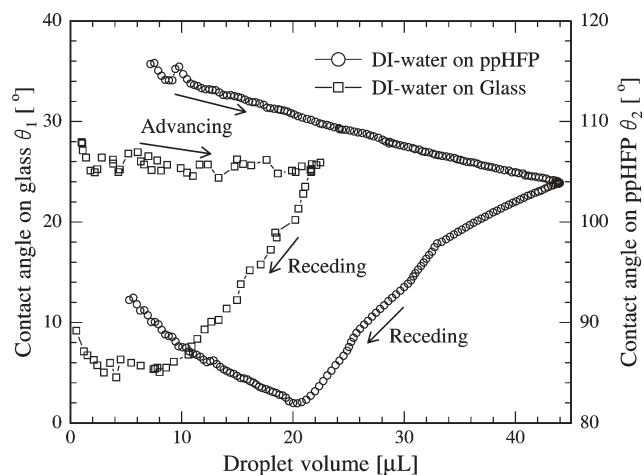


Fig. 4 Advancing and receding water contact angle as a function of droplet volume on ppHFP and glass. The graphs consist of 245 and 78 points respectively, measured in continuous runs. The graph for glass consists of fewer points due to limitations of the contact angle analyzer, *i.e.*, because of a low contact angle. Both measurements were performed using DI water at room temperature, at an air humidity of approximately 40%RH and using spherical and non-spherical fits as contact angle models respectively.

compared to, for instance, measurements on hydrophobic surfaces. The observed fluctuations are therefore not a result of uneven advancing and receding contact angles, but probably due to the limitations of the equipment. The observed advancing contact angle is more or less constant at approximately 25°, whereas the receding contact angle drops from 25° down to approximately 6°, then increases again to approximately 9°. The contact angle on glass generally varies dramatically depending on cleanliness and wetting conditions. To ensure a realistic contact angle, measurements were performed shortly before each set of flow recordings as mentioned above.

The static water contact angle was also measured using the same contact angle analyzer. The static contact angle corresponds approximately to the contact angle at the turning point between the advancing and the receding contact angle, *i.e.*, ~105° and ~25° on ppHFP and glass, respectively. These are within the standard deviations of the measured static contact angles shown in Table 1 (in the case of Experiments 1–3).

4.2 Flow experiments

The flow experiments were performed on meander-like hydrophilic tracks in order to accommodate a long capillary path on a limited sample size. Fig. 5(a) shows a microscope image of the liquid meniscus in a 200 µm wide track, the image was taken using a Leica MZ125 zoom microscope. The curved sections of the track are semicircular arcs with an inner radius of 400 µm. The liquid is obviously confined to the hydrophilic pathway. A close-up image of the front of the liquid meniscus is shown as an insert in Fig. 5(a). The shape of the front meniscus is similar to the shape obtained by FVM simulation, as shown in Fig. 5(b). A similar curvature at the top (lid) of the front meniscus is seen in the two images. This curvature results

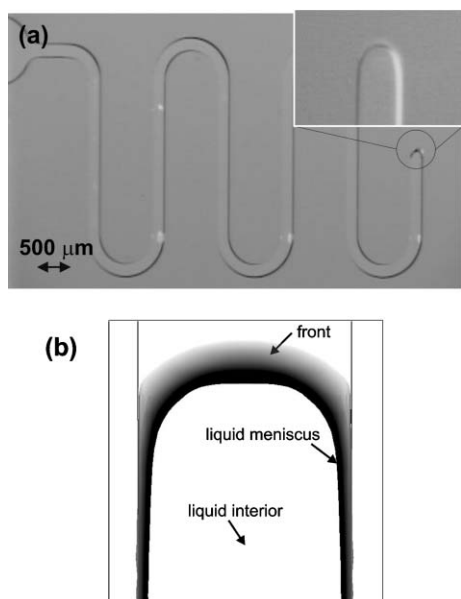


Fig. 5 (a) Microscope image of the liquid meniscus inside a meander-like surface-directed flow system. The width, b , of the hydrophilic zone is $200\ \mu\text{m}$ and the height, a , is $30\ \mu\text{m}$. A close-up of the front of the liquid meniscus is shown in the upper right corner. (b) Result of a FVM CFD-ACE+ simulation, showing the front and sides of the liquid meniscus in the surface-directed flow structure. The liquid film height at the meniscus is grey-scale encoded. The curved shape of the front of the liquid meniscus is similar to the results of the CFD-ACE+ simulation shown in (b).

from minimization of the surface tension energy. The bottom (at the substrate) of the front meniscus however, apparently has a somewhat different shape in the microscope image when compared to the FVM simulation. This difference in appearance is most likely due to limited resolution in the microscope image, since in the simulation a liquid film of any thickness will be visible, whereas a film below a certain thickness is invisible in the microscope.

The arrival time t for the liquid meniscus at predetermined positions x on hydrophilic tracks were determined from video-recorded flow experiments. Details of the experimental conditions, that is the contact angles and channel dimensions are shown in Table 1. Experimental results are shown in Fig. 6 for position as a function of time for two individual, sequential flow experiments on a $200\ \mu\text{m}$ wide and $15\ \mu\text{m}$ high capillary. The two sets of data almost coincide showing the excellent repeatability in the best cases. In some experiments the repeatability was less good, since the contact angles are very sensitive to contamination and since the flow is strongly affected by any particle settling in the capillary. In Fig. 6 the theoretically expected meniscus position according to eqn. (7) is also plotted as the full line. The dashed lines represent the standard deviations due to the experimental uncertainties of the contact angles, θ_1 and θ_2 , and the height, a , which are assumed to be uncorrelated. We have not included uncertainties in the measurement temperature, but these are important since both viscosity and surface tension are strongly temperature dependent. At the measurement temperature the ratio of surface tension to viscosity of water is approximately

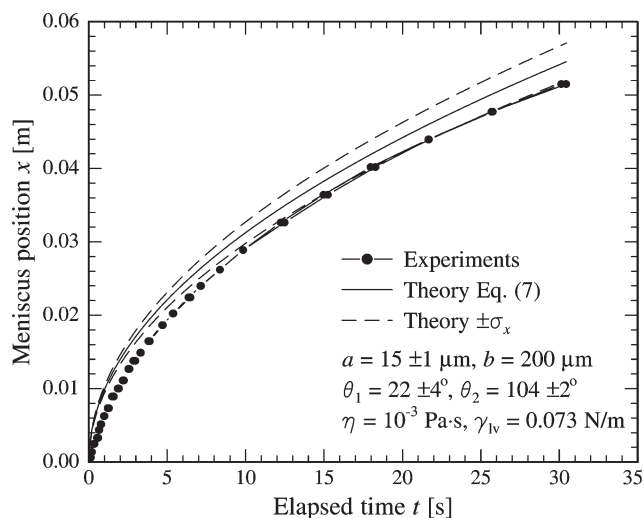


Fig. 6 Experimentally determined meniscus position, x , as a function of time, t , in the microflow system (solid lines with filled circles). The filled circles indicate actual measurements of time and meniscus position for two independent flow experiments. For comparison, the theoretical prediction of the capillary dynamics is shown as a full line, with the standard deviation due to uncertainties in the experimental conditions surrounding it (dashed lines). The dimensions of the flow channel in the experiments are width $b = 200\ \mu\text{m}$ and height $a = 15 \pm 1\ \mu\text{m}$, with the static contact angles $\theta_1 = 22 \pm 4^\circ$ and $\theta_2 = 104 \pm 2^\circ$ for the hydrophilic and hydrophobic surfaces respectively, corresponding to Experiment 1 in Table 1. In the theoretical calculation, a liquid viscosity of $\eta = 10^{-3}\ \text{Pa}\cdot\text{s}$, a liquid surface tension of $\gamma_{\text{lv}} = 0.073\ \text{N}\cdot\text{m}^{-1}$, and a liquid mass density of $\rho = 10^3\ \text{kg}\cdot\text{m}^{-3}$ were assumed.

$\gamma_{\text{lv}}/\eta \approx 73\ \text{m}\cdot\text{s}^{-1}$ with the relative temperature coefficient³⁴ $2.2\% \cdot \text{K}^{-1}$. The actual measurement temperature is not known accurately, since the small, open $50\ \mu\text{L}$ feed volume of DI water might cool significantly due to evaporation during the experiments. In view of these considerations the agreement between the simple theory and the experiments is good ($\sim 5\%$ level).

The theory predicts a meniscus position proportional to the square root time, $x \propto \sqrt{t}$ for large t , see eqn. (8). The square of the experimental meniscus position as a function of time is shown in Fig. 7, where representative data for four different flow experiments, Experiments 1–4 of Table 1, are reported. The experimental positions squared are in all four cases to a good approximation linearly dependent on time as expected, and verified by the linear fits overlaid on the plot (dashed lines).

Eqn. (9) predicts a linear relationship between the aspect ratio a/b of the capillary and the normalized slope, $\beta = (1/a)d(x^2)/dt$, of a plot of the meniscus position squared as a function of time. In Fig. 8 the normalized slopes β for Experiments 1–4 of Table 1, are shown as a function of the aspect ratio a/b of the capillary. At each set of experimental conditions three or four individual experiments were done and these are all reported in Fig. 8. The error bars indicate the measurement errors and the uncertainty related to the channel heights. The full line in the plot shows the theoretical prediction according to eqn. (9) with parameters consistent with the experimental conditions in the Experiments 1–3 of Table 1, whereas the dashed lines indicate the standard

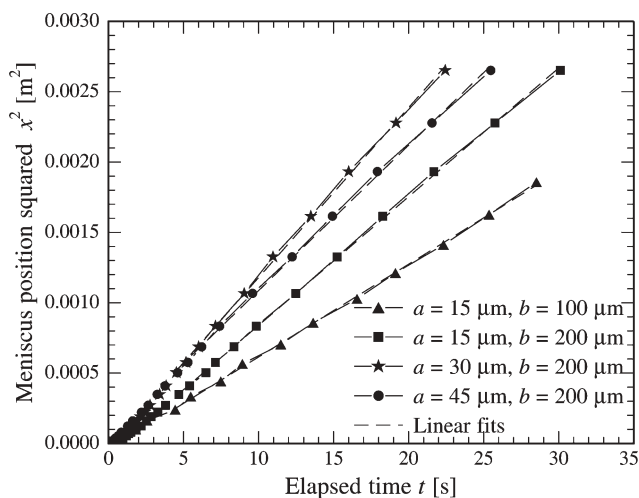


Fig. 7 Experimentally determined values of the square of the position, x^2 , as a function of time, t , for four different flow experiments in the microflow system. The filled symbols represent actual measurements. The four experiments were done with different experimental conditions corresponding to Experiments 1–4 of Table 1. In the experiments the flow system height to width ratios are: ■ $alb = 15 \mu\text{m}/200 \mu\text{m}$, ★ $alb = 30 \mu\text{m}/200 \mu\text{m}$, ● $alb = 45 \mu\text{m}/200 \mu\text{m}$, and ▲ $alb = 15 \mu\text{m}/100 \mu\text{m}$. The dashed lines represent linear fits to the experimental data for each experiment, as expected the linear fits represent the experiments quite well.

deviations corresponding to the uncertainties in the contact angles θ_1 and θ_2 . A linear fit to all the data in Experiments 1–3 of Table 1 essentially coincides with the dashed line corresponding to the lower standard deviation from theory. The slope α of this line only depends on the ratio of surface tension to viscosity of the liquid, $\alpha = -\gamma_{lv}/(3\eta)$. Thus the measurements are in agreement with these parameters at the nominal measurement temperature. The fit line should in theory intersect the abscissa at a value, $\frac{1}{2}(\cos\theta_1 + \cos\theta_2)$, determined only by the contact angles, θ_1 and θ_2 . The intersect of the actual fit is just at the boundary given by the standard deviations of the contact angles. This could be due to the uncertainty in the contact angles in combination with the large uncertainty in the channel height.

The measured flow speeds are consistently below the predicted flow speeds, which is understandable in view of the simplifications involved in the simple theory. The theory clearly underestimates the viscous drag, as discussed in the Theory section, and thus overestimates the flow speed. The meander-like shape of the capillary is also expected to have some impact on the flow speed, since an additional viscous drag is expected from the semicircular arcs. If a simple calculation, based on Poiseuille flow, is done on the capillary flow in a system with an infinite circular track similar to the arcs in the meander structure, the expected slope, β , is 4% less than in a similar linear track. In the flow systems with $b = 200 \mu\text{m}$ 42% of the pathlength is curved, whereas in the case of $b = 100 \mu\text{m}$ only 28% of the pathlength is curved. This difference in geometry might partly explain why the slopes, β , extracted from Experiment 4 ($alb = 15 \mu\text{m}/100 \mu\text{m}$) are significantly ($\sim 14\%$) higher than for Experiment 2 ($alb = 30 \mu\text{m}/200 \mu\text{m}$); the difference in contact angles in the two experiments can

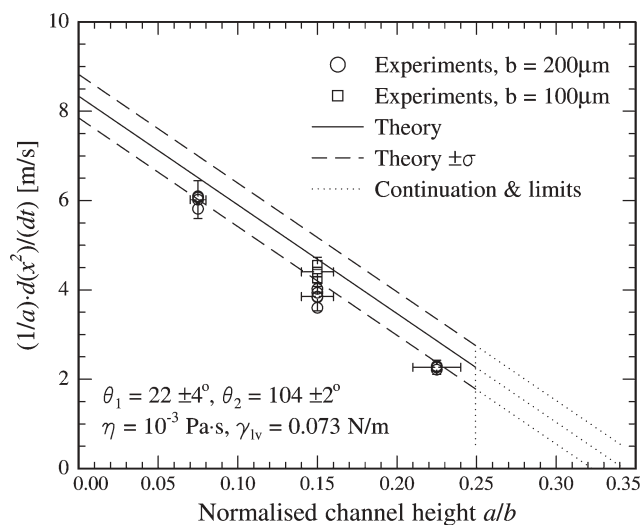


Fig. 8 Experimentally determined values of the time derivative of the meniscus position squared normalized by the channel height, $\beta = (1/a)d(x^2)/dt$, as a function of the normalized channel height a/b . The open symbols represent measurements in four different conditions (Experiments 1–4 in Table 1), for each condition the experiment was repeated three or four times. The symbol □ denotes experiments with the channel width $b = 100 \mu\text{m}$, and the symbol ○ denotes $b = 200 \mu\text{m}$, in both cases the error bars show the combined effect of measurement errors and experimental uncertainties on the channel height. The full line represents the theoretical prediction for experimental conditions corresponding to all the experiments with the channel height $b = 200 \mu\text{m}$ (Experiments 1–3 in Table 1). The dashed lines surrounding it indicate the effect of uncertainties in the actual static contact angles in the experiments. The vertical dotted line indicates the condition where the liquid starts to partially wet the hydrophobic areas surrounding the track. The slanted dotted lines are continuations of the simple theory.

only account for a $\sim 5\%$ increase in slope in Experiment 4. The large uncertainty in capillary height ($\sim 7\%$) might also play a role in explaining the difference between Experiments 2 and 4.

In view of the uncertainties in the experimental conditions, the agreement between experiments and theory is good.

4.3 Human cell experiments

200 μm wide strips of HeLa cells were fabricated using surface-directed flow. The cells were allowed to sediment onto the hydrophilic (glass) pathway inside the flow cell. After 24 hours of incubation, the cells were inspected using the inverted microscope. Fig. 9(a) shows the result of the inspection—a confluent monolayer of cells on the hydrophilic pathway. The liquid meniscus is clearly visible. Fig. 9(b) shows a similar strip of cells after the lid had been removed and the substrate rinsed using PBS, and placed in a Petri dish with conditioned growth medium. The cells still adhere to the hydrophilic pathway. The cells are restricted to the hydrophilic pathways. Also, few cells have attached to the hydrophobic ppHFP generally. The low cell adhesion of ppHFP is in good agreement with previous reports of relatively low biomolecule adsorption, *i.e.*, that ppHFP is non-fouling.^{35–37}

The Petri dish was then placed in the incubator, and after an additional 24 hours of incubation, the growth medium was replaced by the LysoTracker–PBS solution. After 30 min of

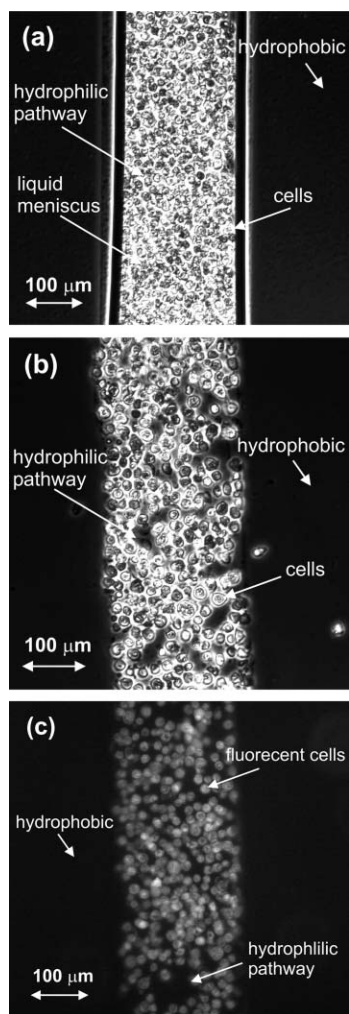


Fig. 9 (a): Optical microscope image of HeLa cells attached to a hydrophilic pathway in a surface-directed flow system. A 100 μm bar is indicated in the lower left corner of the image. The width of the pathway was $b = 200 \mu\text{m}$. The liquid meniscus is clearly visible. The cells form a confluent monolayer inside the flow cell. (b): A similar HeLa cell strip, but after removing the lid of the flow cell. The cells are still attached to the hydrophilic pathway. (c): Cells stained using LysoTracker Red. The cells attached to the hydrophilic pathway are alive.

incubation in the LysoTracker–PBS solution, the substrate was inspected once more. Fig. 9(c) shows the result of the fluorescent staining. The majority of the cells are alive after 48 hours of incubation.

4.4 Protein adsorption experiments

Strips of fluorescence labeled proteins (FITC-BSA) were also fabricated on planar surfaces using surface-directed flow. Fig. 10 shows the result of the adsorption experiments (fluorescent scans). Fig. 10(a) shows FITC-BSA selectively adsorbed onto the hydrophilic pathways on the bottom substrate. Well-defined patterns with high adsorption contrast to the surrounding hydrophobic ppHFP are observed. Fig. 10(b) shows FITC-BSA selectively adsorbed onto the hydrophobic lid, *i.e.*, the areas which were above the

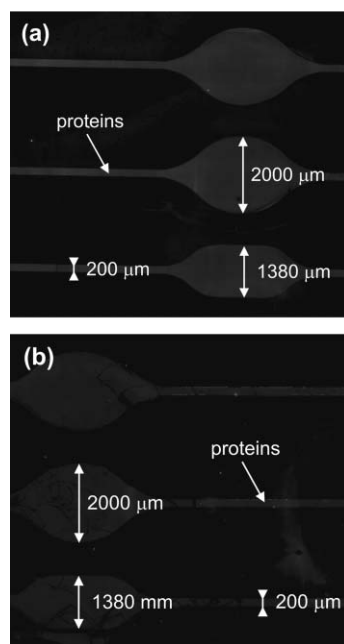


Fig. 10 (a): Result of a fluorescent scan of labeled proteins (FITC-BSA) on the substrate (with hydrophilic pathways). The dimensions are indicated on the figure. The FITC-BSA is selectively adsorbed onto the hydrophilic pathway with minor traces of FITC-BSA scattered across the surrounding hydrophobic ppHFP. (b): Fluorescent scan of the hydrophobic lid (without a hydrophilic pathway). A lower fluorescent intensity is seen, due to poor adhesion of FITC-BSA to the ppHFP.

hydrophilic pathways. A lower fluorescent intensity is seen in this case, due to poorer adhesion on ppHFP compared to glass. This is in good agreement with the cell adhesion results obtained in this study, *i.e.*, low biomolecule adsorption of ppHFP.

In all cases we see minor traces of FITC-BSA scattered across the ppHFP surfaces. This originates from the disassembling of the flow cell, before the fluorescent scan, where FITC-BSA washed out onto the surrounding (hydrophobic) ppHFP areas. With further washing of the surfaces and careful disassembling, the amount of residues would be reduced significantly.

5 Conclusions

An open-channel microfluidic system has been presented. The system consists of parallel planar surfaces separated by spacers, and thus has no sidewalls. The liquid flows on a hydrophilic pathway on the bottom surface, without propagating sideways into surrounding hydrophobic areas. The entire top surface is hydrophobic, which eliminates the need for alignment. The surface-directed flow system was fabricated by patterning (photolithographic lift-off process) of a hydrophobic fluorinated polymer (hexafluoropropene), deposited by plasma-polymerization. The resulting exposed untreated glass areas of the substrate, constitute the hydrophilic pathways.

A theoretical model describing the capillary flow in the system has been suggested and an analytical solution of it was found. The solution is in good agreement with the

experimental results. The minor discrepancies between the theoretical and experimental results were primarily ascribed to four reasons. (1) Geometry, our theoretical model does not take into account the meander-like geometry used in the actual flow experiments. (2) Temperature; the water temperature may have been lower than assumed, resulting in a higher viscosity and lower surface tension. (3) Water contamination; even minute amounts of contaminants may change (decrease) the surface tension. (4) Model assumptions; Poiseuille flow and a simple rectangular meniscus geometry were assumed in the theoretical model.

Biochip applications were demonstrated by fabricating 200 μm wide strips of human (HeLa) cells using surface-directed flow. Confluent monolayers of cells were formed on the hydrophilic pathways. The cell adhesion was tested by removing the lid and flushing the surface with PBS. The cells adhered nicely to the surface, and LysoTracker Red experiments confirmed that the cells were alive.

Fluorescent labeled proteins (FITC-BSA) were also patterned using surface-directed flow. FITC-BSA were selectively adsorbed to both the hydrophilic pathway and the hydrophobic lid, *i.e.*, the area above the hydrophilic pathway. The protein adsorption was however substantially lower in the case of ppHFP, compared to the hydrophilic glass. This was in good agreement with the results obtained for the human cells, where cells on the pathways were not able to form cell extensions into the surrounding ppHFP.

The open sidewalls of the channels in surface-directed capillary flow systems eliminate the problems with air-bubbles seen in conventional closed wall microsystems. In systems handling live cells the easy transport of oxygen and carbon dioxide across the gas/liquid interface is advantageous; moreover this interface also facilitates controlled gas liquid reactions. In some systems the need for other pumping mechanisms besides the capillarity is eliminated, however, if a pressure driven system is required the open channel structure severely limits the maximum pressure allowed, especially in the single sided system presented here.

Acknowledgements

The authors would like to acknowledge Bent Overby for depositing ppHFP coatings. This study was supported by the Danish Academy of Technical Sciences (ATV), project nr. EF946.

References

- 1 D. K. Jones, C. H. Mastrangelo, M. A. Burns and D. T. Burke, Selective Hydrophobic and Hydrophilic Texturing of Surfaces Using Photolithographic Photodeposition of Polymers, *SPIE Conference on Microfluidic Devices and Systems, Santa Clara, CA, SPIE, Bellingham, WA, 1998*, pp. 136–143.
- 2 V. Seidemann, S. Butefisch and S. Buttenbach, Application and investigation of in-plane compliant SU8-structures for MEMS, *Transducers'01: Proceedings of the International Solid-State Sensors and Actuators Conference*, Springer-Verlag, 2001, pp. 1616–1619.
- 3 A. Manz, C. S. Effenhauser, N. Burggraf, D. J. Harrison, K. Seiler and K. Fluri, Electroosmotic pumping and electrophoretic separations for miniaturized chemical analysis systems, *J. Micromech. Microeng.*, 1994, **4**, 4, 257–265.
- 4 S. F. Bart, L. S. Tavrow, M. Mehregany and J. H. Lang, Microfabricated electrohydrodynamic pumps, *Transducers'89: Proceedings of the 5th International Conference on Solid-State Sensors and Actuators and Eurosensors III*, 1989, **21**, pp. 193–197.
- 5 J. Lee, H. Moon, J. Fowler, K. Ghang-Jin and T. Schoelhammer, Addressable micro liquid handling by electric control of surface tension, *MEMS'01: Proceedings of the 14th IEEE International Conference on Micro Electro Mechanical Systems*, IEEE, New York, 2001, pp. 499–502.
- 6 R. Zengerle, A. Richter, H. Sandmaier, W. Benecke and H. C. Petzold, A micro membrane pump with electrostatic actuation, *MEMS'92 Proceedings: An Investigation of Micro Structures, Sensors, Actuators, Machines and Robot*, IEEE, New York, 1992, pp. 19–24.
- 7 J. H. Tsai and L. Lin, A thermal bubble actuated micro nozzle-diffuser pump, *MEMS'01: Proceedings of the 14th IEEE International Conference on Micro Electro Mechanical Systems*, IEEE, New York, 2001, pp. 409–412.
- 8 A. S. Dewa, K. Deng, D. C. Ritter, C. Bonham, H. Guckel and S. Massood-Ansari, Development of LIGA-fabricated, self-priming, in-line gear pumps, *Transducers'97: Proceedings of the International Solid-State Sensors and Actuators Conference*, IEEE, New York, 1997, pp. 757–760.
- 9 R. F. Probst, *Physicochemical hydrodynamics: An introduction*, John Wiley and Sons, New York, 2nd edn., 1985.
- 10 M. Nordstrom, R. Marie, M. Calleja and A. Boisen, Rendering SU-8 hydrophilic to facilitate use in micro channel fabrication, *J. Micromech. Microeng.*, 2004, **14**, 12, 1614–1617.
- 11 S. K. Jong, H. Yang, H.-B. Pyo, K. H. Chung, S. J. Kim and Y. T. Kim, A polymer-based microfluidic device for immunosensing biochips, *Lab Chip*, 2003, **3**, 106–113.
- 12 T. Crowley, M. Hayes and V. Pizziconi, Design of a passive bioseparation microfluidic device, *J. Assoc. Lab. Automat.*, 2003, **8**, 2, 78–80.
- 13 S. Wilson and S. Howell, High-throughput screening in the diagnostics industry, *Biochem. Soc. Trans.*, 2001, **30**, 794–797.
- 14 B. Zhao, J. S. Moore and D. Beebe, Surface-directed flow inside microchannels, *Science*, 2001, **291**, 5506, 1023–1026.
- 15 B. Zhao, J. S. Moore and D. Beebe, Principles of surface-directed liquid flow in microfluidic channels, *Anal. Chem.*, 2002, **74**, 4259–4268.
- 16 P. Lam, K. J. Wynne and G. E. Wnek, Surface tension-confined microfluidics, *Langmuir*, 2002, **18**, 3, 948–951.
- 17 J. D. Quenisset, C. Jama, O. Dessaux and P. Goudmand, Cold plasma fluorination processes of polyethylene surfaces, *Proceedings of the 1997 11th International Colloquium on Plasma Processes, CIP, Soc Francaise du Vide, Paris, 1997*, **284**, pp. 90–93.
- 18 F. Garbassi and E. Occhiello, Surface modification of PAN fibers by plasma polymerization, *J. Adhes. Sci. Technol.*, 1999, **13**, 1, 65–78.
- 19 J. W. Stansbury and J. M. Antonucci, Dimethacrylate monomers with varied fluorine contents and distributions, *Dent. Mater.*, 1999, **15**, 166–173.
- 20 L. Jones and K. Doblhofer, Electrochemical characterization of the permeability and the loss of adhesion of plasma-polymerized hexafluoropropene films on platinum, *Werkst. Korros.*, 1991, **42**, 6, 309–316.
- 21 H. F. Knapp and A. Stemmer, Preparation, comparison and performance of hydrophobic AFM tips, *Proceedings of the 1998 SPM-3 Conference on Development and Industrial Application of Scanning Probe Methods*, John Wiley and Sons, New York, 1999, **27**, 5, pp. 324–331.
- 22 Y. J. Wu, R. B. Timmons, J. S. Jen and F. E. Molock, Non-fouling surfaces produced by gas phase pulsed plasma polymerization of an ultra low molecular weight ethylene oxide containing monomer, *Colloids Surf. B: Biointerfaces*, 2000, **18**, 235–248.
- 23 Y. Hanein, Y. V. Pan, B. D. Ratner, D. D. Denton and K. F. Böhringer, Micromachining of non-fouling coatings for bio-MEMS applications, *Sens. Actuators, A*, 2001, **81**, 49–54.
- 24 Y. V. Pan, Y. Hanein, D. Leach-Scampavia, F. K. Böhringer, B. D. Ratner and D. D. Denton, A precision technology for controlling protein adsorption and cell adhesion in bioMEMS, *14th IEEE International Conference on Micro Electro Mechanical Systems (MEMS), Interlaken, Switzerland, Jan 2001*, IEEE, New York, 2001, pp. 435–438.

-
- 25 Y. V. Pan, T. C. McDevitt, T. K. Kim, D. Leach-Scampavia, P. S. Stayton, D. D. Denton and B. D. Ratner, Micro-scale cell patterning on nonfouling plasma polymerized tetraglyme coatings by protein microcontact printing, *Plasmas Polym.*, 2002, **7**, 2, 171–183.
- 26 W. J. van Ooij, S. Eufinger and S. Guo, DC Plasma polymerization of hexamethyldisiloxane, *Plasma Chem. Plasma Process.*, 1997, **17**, 2, 123–154.
- 27 S. Bouaidat, B. Winther-Jensen, S. F. Christensen and J. Jonsmann, Plasma-polymerized coatings for bio-MEMS applications, *Sens. Actuators, A*, 2004, **110**, 390–394.
- 28 S. Bouaidat, C. Berendsen, P. Thomsen, S. G. Petersen, A. Wolff and J. Jonsmann, Micropatterning of cell and protein non-adhesive plasma polymerized coatings for biochip applications, *Lab Chip*, 2004, **4**, 632–637.
- 29 F. Brochard-Wyart, Droplets: capillarity and wetting, *Soft Matter Phys.*, 1999, **335**, 1–45.
- 30 R. W. Fox and A. T. McDonald, *Introduction to fluid mechanics*, John Wiley and Sons, New York, 3rd edn., 1985, ch. 2, p. 29.
- 31 F. M. White, *Viscous fluid flow*, McGraw-Hill Inc., New York, 2nd edn., 1991, ch. 3, p. 119.
- 32 B. V. Zhmud, F. Tiberg and K. Hallstensson, Dynamics of capillary rise, *J. Colloid Interface Sci.*, 2000, **228**, 263–269.
- 33 P. Thomsen, B. van Deurs, B. Norrild and L. Kayser, The HPV16 E5 oncogene inhibits endocytic trafficking, *Oncogene*, 2000, **19**, 52, 6023–6032.
- 34 F. M. White, *Viscous fluid flow*, McGraw-Hill Inc., New York, 2nd edn., 1991, p. 51 and p. 565.
- 35 M. Kanai, D. Uchida, S. Sugiura, Y. Shirasaki, J. S. Go, H. Nakanishi, T. Funatsu and S. Shoji, PDMS Microfluidic devices with PTFE passivated channels. *7th International Conference on Miniaturized Chemical and Biochemical Analysis Systems, Squaw Valley, USA, October 2003*, RSC, London, 2003, pp. 429–432.
- 36 D. J. Balazs, C. Hollenstein and H. J. Mathieu, Surface modification of poly(vinyl chloride) intubation teflon-like and pluronics, *Eur. Cells Mater.*, 2002, **3**, 1, 7–8.
- 37 M. A. Malangoni, D. H. Livingston and J. C. Peyton, The effect of protein binding on the adherence of staphylococci to prosthetic vascular grafts, *J. Surg. Res.*, 1993, **54**, 2, 168–172.